International Journal of Rock Mechanics & Mining Sciences 157 (2022) 105171

Contents lists available at ScienceDirect

International Journal of Rock Mechanics and Mining Sciences

journal homepage: www.elsevier.com/locate/ijrmms

Analysis of slope fracturing under transient earthquake loading by random discrete element method

Tao Zhao [a,c,*], Giovanni B. Crosta [b], Yong Liu [c]

[a] Department of Civil and Environmental Engineering, Brunel University London, London, UB8 3PH, United Kingdom
[b] Department of Earth and Environmental Sciences, Università degli Studi di Milano Bicocca, Piazza della Scienza 4, 20126, Milan, Italy
[c] State Key Laboratory of Water Resources and Hydropower Engineering Science, Institute of Engineering Risk and Disaster Prevention, Wuhan University, 299 Bayi Road, Wuhan, 430072, PR China

ARTICLE INFO

Keywords:
Earthquake
Slope fracturing
Random field theory
DEM
Ground motion amplification
Seismic energy

ABSTRACT

Earthquake can cause significant rock fracturing in either the short or long terms. A comprehensive analysis of the fracturing mechanism is critical for assessing the risks of potential slope failures, landslides and rock avalanches in seismic prone areas. This study employed 2D discrete element method (DEM) to investigate the fracturing of an intact rock slope of 600 m in base length and 300 m in height, with explicit considerations of material heterogeneity by random field theory. A total of 5400 DEM simulations were performed, and the characteristics of slope fracturing were statistically analysed. The dynamic loading by earthquake has triggered significant amplifications of ground motion and slope damage at the slope crest, resulting in densely spaced and interconnect fractures. These fractures split the slope into a collection of rock fragments with varied shapes, and the fragment size followed the Weibull's cumulative distribution. More than 70% of generated fragments were finer than 0.1 times the initial slope size, while only few large fragments existed at the slope base. The fragment size distribution pattern could quantitatively agree with field observations. The distributions of final slope damage index and cumulated fragmentation energy all followed the normal distribution pattern. The overall bulk seismic energy input into the slope was dissipated mainly at discontinuities and decreased with the increase of slope inclination.

1. Introduction

Slope failures triggered by strong earthquakes have been observed worldwide close to the main earthquake fault zones.[1–4] The earthquake-induced ground shaking provides additional kinetic energy for slope destabilization, which can quickly loosen and weaken the slope materials.[5] It is highly efficient in deforming and fracturing rock masses leading to the progressive slope failure.[6] As a result, slopes can be gradually shattered and finally collapse to spread almost instantaneous at high speeds, posing extreme risks to local communities and natural environment.[7–11] These processes occur frequently and concentrate in regions of strong ground motions and decay quickly with the distance from the epicentre.[8,12–14] As stated in Ref. 15; the landslide occurrence rate peaks after a major earthquake event and decays gradually with time, with the time scale proportional to earthquake magnitude. For example, the 2008 Ms 8.0 Wenchuan earthquake in China has triggered more than 60,000 landslides in the Longmenshan fault zone,[16] and the 2015 7.8 M_w Gorkha earthquake in Nepal has triggered over 21,000 landslides,[17] leading to significant loss of human lives and properties. The subsequent secondary hazards, such as debris flows and landslides, can last for a relatively long period of time as a huge number of earthquake-induced fractures and cracks in slopes pre-condition geo--hazards in snowmelt or rainy and monsoon seasons.[18–21] Furthermore, it is expected that ground shaking and consequent rock mass damage control both volume and grain size of debris available for transport in rivers, affecting the river geometry and transport capacity in downstream regions.[22]

In the past several decades, great efforts have been devoted to study the mechanism of slope failure and the subsequent runout, while little has been done to investigate the slope fracturing process. Site investigations have shown that the seismic impact could create or activate a huge number of persistent discontinuities and pre-existing open fault planes in the upper portion of the slope, while the slope toe region can remain relatively intact.[23] This is due mainly to site effects amplifying

* Corresponding author. Department of Civil and Environmental Engineering, Brunel University London, London, UB8 3PH, United Kingdom.
E-mail address: tao.zhao@brunel.ac.uk (T. Zhao).

https://doi.org/10.1016/j.ijrmms.2022.105171
Received 3 December 2021; Received in revised form 13 April 2022; Accepted 11 July 2022
Available online 30 July 2022

the ground motion near the crest and consequently most coseismic landslides mainly occur in the upper slope sectors.[11,13] As stated in Ref. 24, earthquake shaking can effectively loosen and weaken the slope, facilitating the infiltration of water during rainfall. The weathering by water infiltration can reduce effectively the strength of slope materials.[25] As a result, the material strength becomes highly heterogeneous and increases with depth.[26] These conditions are crucial for subsequent catastrophic landslides occurring in the upper slope sector, where strong shaking, unloading and weathering effects are dominant. Due to the long recurrence time and unpredictable nature of earthquakes, direct field-based investigations of their impact on slope damage and failure are difficult, and numerical simulations can be an effective research method forward. Gischig et al.[27] investigated the mechanism of seismically induced rock mass damage and its influence on slope progressive failure via 2D distinct-element modellings (DEM). Their results confirmed the important role of repeated earthquake activity over time in destabilizing a strong and competent rock slope by progressive fracturing. The pre-existing slope damages were found to dominate the fracturing and displacement that a certain earthquake can cause. The slope fracturing and post-failure landslide dynamics were further analysed by Zhao & Crosta[28] using the 3D DEM simulations, showing the slope failure at the peak ground seismic acceleration when a sudden increase of tensile and shear stresses damaged the particle cementations.

For numerical simulations, most traditional slope stability and landslide dynamics models, such as the limit equilibrium method, finite element and meshfree analysis, have neglected or not properly account the spatial variability of material properties due partly to the convenience of model configurations.[29] Though these simplified models may capture some features of specific slope failure events, they cannot quantify the spatial variability and uncertainty of material properties (e.g. strength, elastic modulus, fracture distribution and permeability). The spatial heterogeneity affects crucially how and where a slope may fail under external loadings. For example, under earthquake impacts, a slope may fail preferentially along the weak zones as the locally concentrated stress can easily exceed the material strength. As a result, these models may produce unrealistically high/low probabilities of slope failure, leading to costly engineering design or highly risky constructions. Recent advancements in numerical modelling employ the random field theory (RFT) to investigate the variability of slope properties as multi-dimensional and multi-variate random fields.[30] Considering the discontinuous nature of geomaterials, the RFT has been coupled with DEM to study the fracturing and large deformation processes of heterogeneous rock masses.[31]

Therefore, an in-depth understanding of slope fracturing mechanism and its influence on slope stability and landscape evolutions under seismic loading is highly necessary. In this respect, the current research has employed an RFT-DEM coupling approach to investigate the response of a rocky slope under transient earthquake loading. The paper is organized as follows: in section 2, the RFT-DEM theory and model configuration are illustrated. In section 3, the obtained numerical results of seismic induced slope fracturing process are presented. Section 4 presents the discussions on modelling timescale, slope fragmentation and multiple earthquake impacts.

2. Methodology and model configuration

2.1. RFT-DEM theory

The RFT-DEM coupling model was developed based on the open-source DEM code ESyS-Particle.[32] In DEM, the dynamics of each individual particle is governed by the Newton's second law of motion and the interactions between particles are computed by a simple linear elastic spring contact model. The rocky slope is represented as a collection of densely packed spherical rigid particles, which are stressed under gravity and cemented together by the so-called parallel bond model (PBM).[33,34] In the PBM model, the bonding forces are computed by the linear-elastic spring model and the relative displacements are obtained through the representation of spatial rotation by unit quaternions. The interparticle cementation (i.e. bond in DEM) would break when the combined loads exceed its bonding strength capacity, as determined by Eq. (1):

$$\frac{F_{bn}}{F_{bnMax}}+\frac{F_{bs}}{F_{bsMax}}+\frac{M_b}{M_{bMax}}+\frac{M_t}{M_{tMax}}\geq 1 \tag{1}$$

where F_{bn}, F_{bs}, M_b and M_t are the normal, shear forces, bending and twisting moments between the two bonded particles; F_{bnMax}, F_{bsMax}, M_{bMax} and M_{tMax} are the bonding strengths in the normal, shear, bending and twisting directions, respectively. Based on this model, the slope internal fractures would occur naturally when the loading stress exceeds the particle bonding strength at any specific location. This approach avoids the use of some phenomenological constitutive laws, such as those used in conventional continuum modelling.

Once the interparticle bond breaks, the particles become dispersed and interact with each other via the linear-elastic spring contact model and interparticle friction. The related fundamental DEM theory and rigorous calibrations can be found in Ref. 35 and will not be repeated herein.

In DEM, the total potential energy (E_p) of a granular system is defined as the summation of the potential energy of individual particles with respect to the elevation base, as:

$$E_p=\sum_{i=1}^{N} m_i g H_i \tag{2}$$

where N is the total number of particles in the model; m_i and H_i are the mass and elevation height of a particle i, respectively; g = 9.81 m/s^2 is the gravitational acceleration.

The kinetic energy is calculated as the summation of the translational and rotational kinetic energy of all particles in the granular system,

$$E_k=\frac{1}{2}\sum_{i=1}^{N}\left(m_i|v_i|^2+I_i|\omega_i|^2\right) \tag{3}$$

where I_i is the momentum of inertia; v_i and ω_i are the linear and angular velocities of particle i.

The elastic energy stored in each individual bond, E_b, is calculated as follows:

$$E_b=\frac{F_{bn}^2}{2K_{bn}}+\frac{F_{bs}^2}{2K_{bs}}+\frac{M_b^2}{2K_b}+\frac{M_t^2}{2K_t} \tag{4}$$

where K_{bn}, K_{bs}, K_b and K_t are the stiffnesses of interparticle bonding interactions in the normal, shear, bending and twisting directions, as calculated from the Young's modulus and Poisson's ratio of the particle contact and bond.[35] Once a bond breaks (see the criterion in Eq. (1)), its elastic energy (E_b) would be released completely. The released energy was recorded at each iteration time step in the DEM simulation for all broken bonds. The cumulative energy released from the beginning to the current simulation time is defined as the slope fragmentation energy, E_f.

After bond breakage, the elastic energy stored at a particle contact, E_c, is calculated as follows:

$$E_c=\frac{F_n}{2K_n}+\frac{F_s}{2K_s} \tag{5}$$

where F_n, F_s are the normal and shear contact forces; K_n, K_s are the stiffnesses of interparticle contact interaction in the normal and shear directions, respectively.

The cumulative energy dissipation due to frictional and damping forces at particle contacts are computed incrementally as:

$$E_{fric}^{i}=E_{fric}^{i-1}+\sum_{j=1}^{N_c} f_j \Delta u_{sj} \tag{6}$$

$$E_d^i = E_d^{i-1} + \sum_{j=1}^{N_c} F_{dj}\Delta u_{nj} \tag{7}$$

where E_{fric}^i and E_{fric}^{i-1} are the cumulative energy dissipations by friction at the current and previous time steps; f_j and Δu_{sj} are the friction force and incremental sliding displacement for the jth contact; E_d^i and E_d^{i-1} are the cumulative energy dissipations by damping force at the current and previous time steps; F_{dj} and Δu_{nj} are the damping force and incremental normal displacement at contact j; N_c is the total number of particle contacts in the model. To generalize the results, all energy components are normalized by the total initial potential energy (E_{p0}, at the beginning of the simulation).[36]

In RFT, the material properties are considered as a series of random values initially generated at the nodal points of the discretized staggered domain grids, following the standard Gaussian distribution pattern. Then, the exact material properties at the discrete particle centres are estimated linearly based on the values at the surrounding nodal points, through a series of randomized translations and rotations from one realization to the next.[30] In this approach, these random values are mutually correlated by a specified correlation length (i.e. scale of fluctuation), such that the properties of adjacent soil particles as variables within this length scale do not differ too much as those further apart. Once the random fields are generated, they are imported into DEM as the distribution of initial material properties of the slope model. In this research, 5400 DEM simulations have been performed on the same granular assembly, but with different realizations of slope properties. It is assumed that the number of simulations is large enough for obtaining statistically reliable results.

2.2. Model configuration

The inclination of natural rock slopes could range from about 30° for very poor-quality rock masses to near vertical for shallow pits or rocky cliffs in good-quality rock.[37] Inclination has been reported as one of the controlling factors in rock slope design. In this research, a fixed slope inclination angle of 60° was first used in DEM simulations to investigate the slope material heterogeneity effects. The crest width and volume of this slope were denoted as w_0 and V_0. Then, the slope geometric effects were analysed by varying the slope inclination angle from 30° to 90° to account for the wide range of slope inclinations of natural slopes, while maintaining either a constant crest width (as w_0) or a constant slope volume (as V_0). In these tests, the slope height was kept constant as 300 m.

The slope inclined at 60° had a symmetrical isosceles trapezoid shape with the dimensions of 600 m in base length and 300 m in height (see Fig. 1 (a, c)). The slope geometry was configured according to the field observations by Elsen & Tingley[38] that most of the mountains have the "hourglass" shape, where they slope steeply upwards, before flattening out into broad high plains. Indeed, the adopted slope geometry is far simpler than the reality. However, it can effectively reduce the influence of irregular slope topography on the dynamics of slope failure during seismic wave propagations. In this study, a 2D simulation condition is adopted in order to better visualize the fracturing process while reducing the computational cost. The 2D simulations have been widely used in slope stability analyses[6,27,39] to provide initial results on slope evolution.

The rocky slope consists of densely packed spherical particles of diameters in a narrow range of [1.9, 2.0] m. These particles have sizes comparable to real rock mass blocks, and the interparticle bond could effectively represent the rock bridges between adjacent blocks/particles, contributing some cohesion to the rock mass.[28] The rock type is assumed to be sandstones which are typical for landslides and rock avalanches occurred during/after the 2008 Wenchuan earthquake in Southwest China.[40] In an idealized rocky slope, the mean particle bonding strength ($\bar{c}$) is assumed to increase linearly with depth and distance from the slope surface to account for the strength degradation due to weathering, as with various field investigation results.[26,41,42] As one of the key geomechanical parameters, the uniaxial compression strength (*UCS*) of rock is considered to have the most significant influence on slope stability.[39] In this study, the peak value of mean particle bonding strength ($\bar{c}$) at the slope base was set as 82.5 MPa according to the published

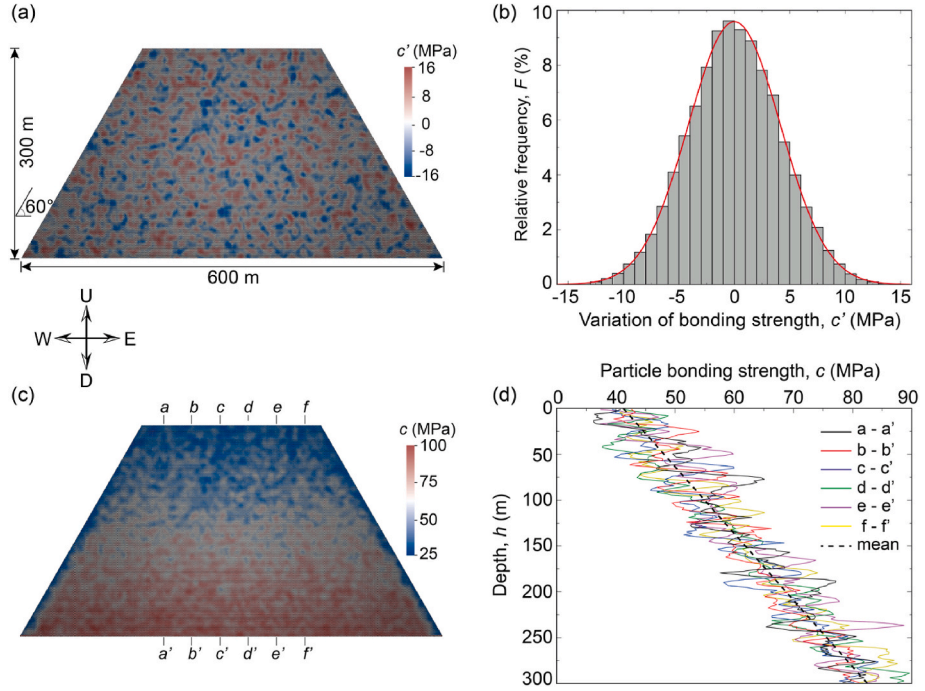

Fig. 1. (a) A typical random field of the particle bonding strength variation (c'). (b) The statistics of bonding strength variation in (a) fitted by the normal distribution function. (c) The distribution of exact particle bonding strength in the slope. (d) Variations of particle bonding strength along the depth at 6 representative cross-sections in (c). The black dashed line shows the variation of mean strength along the depth. The directions are defined as, E: East, W: West, U: Up, D: Down.

experimental data of sandstone uniaxial compression strength.[43] However, due to the heterogeneity of slope formation (e.g. fractures and weak layers), the rock strength varies widely within the slope and the weak zones normally have much lower strengths than the mean value. It has been reported that the UCS of sandstone can span a wide range from 5 MPa to over 150 MPa, depending on the local material conditions, such as composition, porosity, cementation and saturation.[44] To consider this variability, it is assumed that the variation of particle bonding strength (c') in DEM is 20% of the peak bonding strength, as represented by a typical random field in Fig. 1(a). The exact particle bonding strength (c) is thus computed as $c = \bar{c} + c'$, as shown in Fig. 1(c) for a possible distribution. The corresponding variations of particle bonding strength along the depth at six representative cross-sections are shown in Fig. 1(d). The curves clearly show the fluctuation of particle bonding strengths about the mean value, which is similar to typical site investigation results.[26,45,46]

The spatial correlation length of c' was set as 10 m, which accounts for the existing published data in a wide range of 0.1–200 m[46,47] and the relatively large particle size (~2 m) used in the DEM model. The distribution of the random variable c' follows well the standard normal distribution as shown Fig. 1(b). According to Ref. 48, using the intermediate value of correlation length, the slope is not homogeneous and anomalies, such that the locations of weak zones would effectively control the probability of slope failure. In this work, the DEM analysis can "seek out" the weakest path through the slope during the fracturing process. As this study mainly focuses on the characteristics of slope fracturing for a typical model configuration, the sensitivity of spatial correlation length on the slope fracturing process is not analysed. However, it is apparent that this parameter will influence the characteristics of slope fractures. To simplify the analysis, the elastic moduli of particle bonding and contacts are set the same as a constant value of 10.5 GPa.

Fig. 2 shows the ground accelerations and displacements used in the DEM simulations, which is modified from the Wenchuan earthquake records obtained from the seismic station at Qingping town (31.54564°N, 104.1142°E, Mianzhu County, China). The peak ground acceleration (PGA) recorded in the EW and UD directions were 0.84 g and 0.63 g, respectively (see Fig. 2(a)). To shorten the simulation time, the intense ground shaking period of the original 50 s was reframed into a 5-s period. This approach effectively speeds up the DEM simulation by 10 times. The raw data of ground acceleration was first processed by high-pass filter (with the cut-off frequency in the range of [0.2, 20] Hz) and baseline correction to remove the signal noise. Then, the accelerations were double integrated to produce the ground displacements. For the 2D DEM simulations, the EW and UD components of ground displacements were applied at the base of the slope in the horizontal and vertical directions as the movable boundary conditions. Though discrepancy between numerical simulation and field data exists, the DEM model can effectively capture the continuous ground shaking at a relatively low computational cost. It is assumed that this approach can reveal the general characteristics of seismic induced slope fracturing process.

3. Results

In the analysis, the evolution of slope fracturing induced by a transient earthquake for simulations using different material strengths and slope geometries were investigated. The DEM simulation using uniform interparticle bonding strengths (i.e. no random variation introduced) was also included (termed "uniform slope") for comparison purpose. An idealized intact and unbreakable uniform slope was used in analysing the ground amplification effects, while the brittle slopes (both heterogeneous and uniform slopes) were used in the rest of analyses. The results will be presented in terms of damage index (D), nominal fragment size (d) and slope energy components.

3.1. Ground displacement

The ground amplification effect at different locations of an intact slope can provide useful information on where and how the cracks would occur. To understand this, an unbreakable uniform slope was employed in the DEM simulations using an extremely high interparticle bonding strength (i.e. 10^{10} GPa), such that no bond breakage was allowed during the simulation. Fig. 3 shows the predicted cumulative ground displacement at seven different measurement locations at the base (B1), middle (M1, M2, M3) and top (T1, T2, T3) sectors of the slope, respectively. The displacement at the slope base (B1) corresponds to the input of the movable DEM boundary condition. For both the EW and UD directions, the ground displacement increased with the height and the slope surface normally had much larger displacements than the inner slope. The strongest ground displacement amplification occurred during 1–2.5s, when intense base excitations were persistent. The peak magnitudes of ground surface displacements occurred at the slope crest surface and were up to 8 times the slope base displacements in the EW and UD directions, respectively. The peak values always occurred shortly after the base excitation reached its peak, due to the delay of

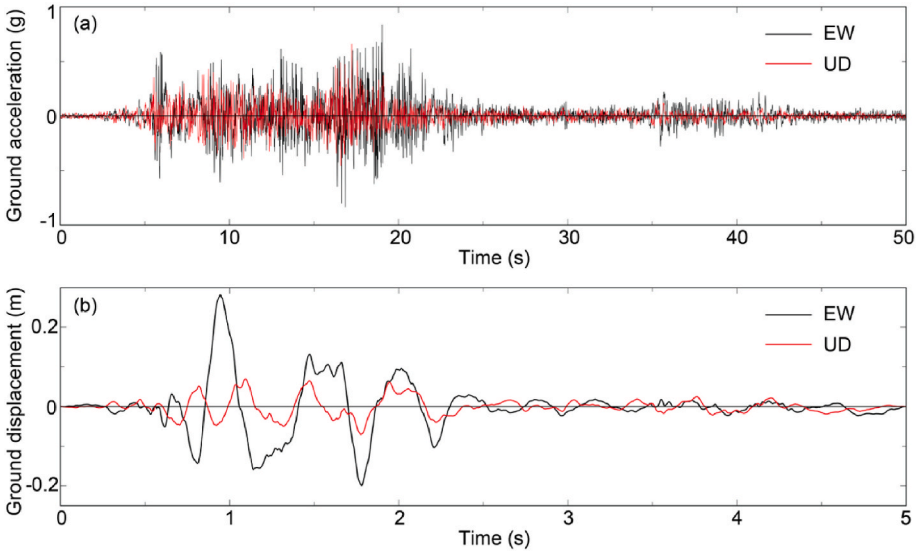

Fig. 2. The ground acceleration (a) and the reframed ground displacement (b) in the EW and UD directions used in the DEM modelling as the boundary conditions at the slope base. The ground acceleration is expressed as the ratio to the gravitational acceleration ($g = 9.81$ m/s^2). The signals were modified from the Wenchuan seismic wave records (Ms = 8.0) at Qingping seismic station (31.54564°N 104.1142°E, Mianzhu County, China) which is 90.75 km from the epicentre (30°57′N, 103°24′E). The records started at 14:28:14 p.m., GMT +8, May 12, 2008. The seismic wave records were provided by the National Earthquake Data Center (http://data.earthquake.cn).

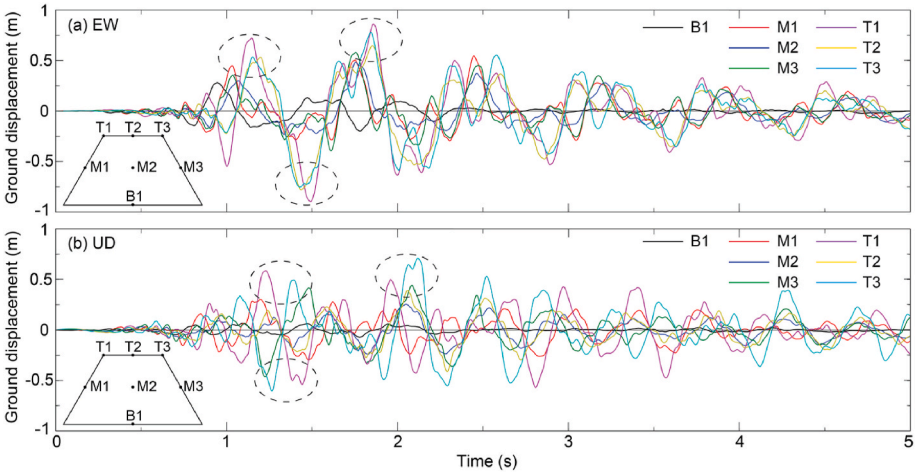

Fig. 3. The (a) EW and (b) UD components of cumulative ground displacement at representative monitoring locations at the bottom (B1), middle height (M1, M2, M3) and top (T1, T2, T3) sectors of the slope. In the series of tests, the slope fractures are not allowed to occur.

elastic wave propagation within the slope. At any specific time, the magnitude and direction of ground displacements of these locations were never synchronized. For the EW component, locations at the same elevation showed very similar pattern (e.g. M1, M2 and M3), despite of small differences in the displacement magnitude. For the UD component, very large differential ground displacements existed at these locations. At some instants (e.g. 1–1.5 s, 2–2.25s), locations at the same elevation height had displacements in completely opposite directions (e.g. T1 and T3). As a result, fractures were likely to occur along the vertical or sub-vertical directions (see the distribution of fractures in Fig. 4). The numerical simulation can qualitatively match the results reported in Ref. 6 that the cumulative slope displacement could be amplified significantly near the slope free surface.

3.2. Characteristics of slope fracturing

Fig. 4 illustrates the evolution of internal fracturing process for a typical heterogenous slope (the input random field of particle bonding strength is shown in Fig. 1(c)). The slope internal damage is quantified by the damage index, *D*, defined as the ratio of the cumulative number of bonds broken during the simulation to the total number of bonds in the model before the test. The damage was firstly initiated at around 1 s near the left crest region where the amplification of ground displacement and ridge effect are significant (see Fig. 3). Once the initial cracks occurred, the subsequent damages would develop preferably close to these existing damaged zones, with a systematic opening of fractures subperpendicular to the slope surface. As stated in Ref. 23, this peculiar pattern of fractures creates meso-scale anisotropy in the bulk rock mass elasticity, such that the slope becomes more deformable parallel to the potential failure direction. As the ground shaking intensity increased, more small cracks occurred in the left and upper regions of the slope. Correspondingly, the damage index increased rapidly from 2.3% to 6.6% within 0.25 s. The cracks propagated preferably along the weak zones along different directions where the interparticle bonds have low strengths in the random field. These small cracks quickly nucleated and grew to completion to form interconnected fracturing zones, which consequently split the slope into a series of rock fragments. Only few cracks occurred at the bottom region of the slope due to the high rock strength and low ground surface amplifications. The slope fracturing process occurred mainly between 1 and 2 s when the ground seismic loading intensity was very high. After t = 2 s, no appreciable new fracture was observed. The open cracks orientated preferentially along the vertical and sub-vertical directions, which is similar to the numerical results reported in Refs. 6,27 and field observations of some giant landslides triggered by the 2008 Wenchuan earthquake in Ref. 49. The occurrence of interconnected and thoroughgoing fractures within the slope (see Fig. 4(c–f)) could potentially lead to subsequent loose mass flow and catastrophic deep-seated landslides, which was classified as "tension-shattering failure" in Ref. 49.

Fig. 5(a) illustrates the evolution of slope damage index (*D*) with time for both heterogeneous and uniform slopes. Before t = 0.6 s, there was no slope damage as the ground shaking intensity was negligibly

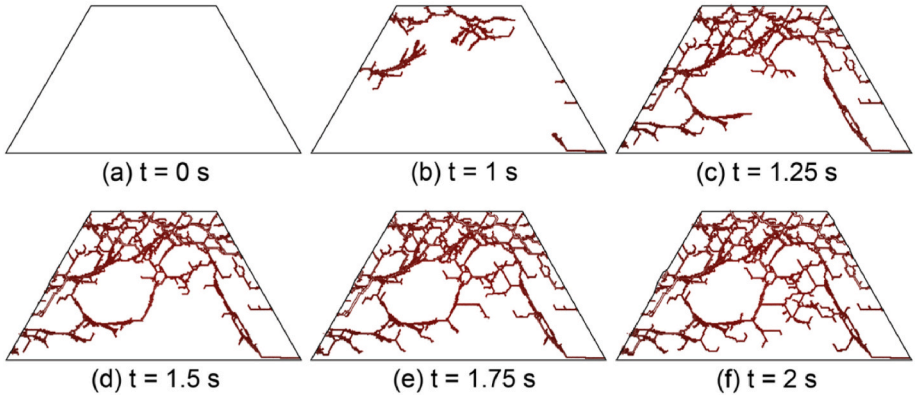

Fig. 4. Evolution of slope internal damage zones for a typical heterogeneous slope (the damage zone is represented by the red dots). The damage index (D) of slope is (a) 0%, (b) 2.3%, (c) 6.6%, (d) 7.4%, (e) 8%, (f) 8.9%. (For interpretation of the references to colour in this figure legend, the reader is referred to the Web version of this article.)

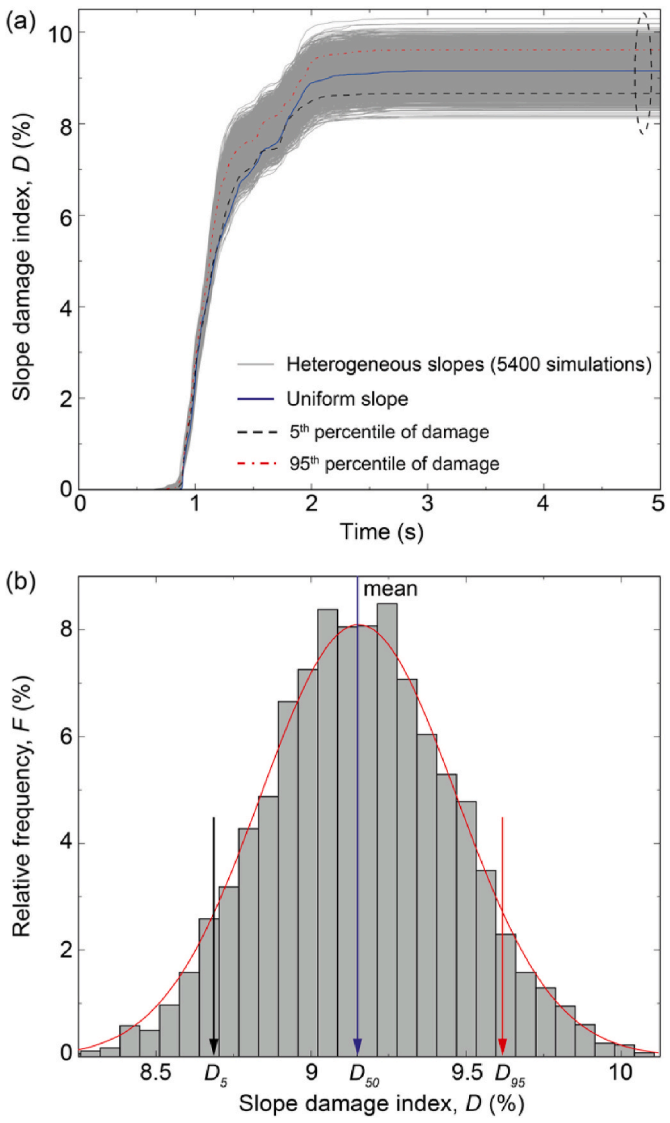

Fig. 5. (a) Evolution of the slope damage index (D) over time. (b) the statistics of slope damage index. D_5, D_{50}, D_{95} represent the final slope damage index at 5th, 50th and 95th percentiles.

small. Then, D increased slightly as the EW component of ground shaking started to increase suddenly, while the UD component still remained very small. The time for slope damage initiation varied for different simulations as determined by the random fields of the particle bonding strength. The uniform slope can effectively resist the fracture initiation and the damage occurred the latest at t = 0.88 s when the ground shaking intensity started to rise abruptly. From t = 0.88 s–1.5 s, D increased almost linearly to reach a relatively high value of about 7%–9%. In this process, the majority of slope damages occurred as a result of intense ground shaking. After t = 1.5 s, D increased slowly even though the ground accelerations were still intense. This is because the widespread fractures can effectively reduce the propagation of seismic wave within the slope. A large portion of slope kinetic energy has been dissipated through bond breakage and the frictional interactions between the rock fragments (see Figure A1 in the Supplementary Information). In addition, some of the rock fragments detaching from the slope would not suffer from any further shaking-induced damages and on the other hand, the remaining slope of strong intact bedrock could also resist the seismic loading. The slope damage index remained unchanged after t = 2.0 s for all simulations. The distribution of the final value of D follows well the normal distribution pattern as shown in Fig. 5(b). The mean value (D_{50}) is 9.15% which approximately equals that of a uniform slope (D = 9.16%), indicating that the simulation using a uniform slope can represent the average characteristics of slope fracturing process. The 5th and 95th percentiles of the final slope damage index in the distribution are 8.66% and 9.66%, respectively. These two values can be used to evaluate the potential risks of subsequent slope failure. To reveal the characteristics of rock fragments, the simulations of 5th, 50th, 95th percentiles of final damage index are further analysed below.

After the earthquake loading, the slope was highly fractured. The widespread discontinuities delineated randomly shaped and sized rock fragments. In the analysis, a granular agglomerate was only considered as a rock fragment if it consisted of more than 10 particles. Fig. 6 illustrates the collection of fragments for the simulations of 5th, 50th, 95th percentiles of final damage index (see Fig. 5(b)) and the uniform slope. For these tests, the largest fragments were consistently found at the slope base, with highly irregular shapes. These fragments were considered as the bedrock under the direct earthquake loading impact. Other fragments had roughly blocky shapes. The fragment size increased with depth, with the majority of fine fragments concentrated near the upper crest region. These fragments can be considered as at high risks of potential falling/detachment if further disturbances such as earthquakes or rainfall occur, because of the relatively high damage intensity and large deformations. The lower region of the slope could fail by translational sliding on stepped surfaces. These numerical findings are in accordance with the field observations reported in Ref. 23. The uniform slope (Fig. 6(d)) had a fragment distribution pattern similar to the heterogeneous slope and the fragment sizes were comparable to those in Fig. 6(b). In the uniform slope, the fragmentation concentrated mainly in several large cracks in the middle and upper sectors of the ridge, with less complete fractures but wider openings than the heterogeneous slopes. Thus, the uniform slope was relatively more stable than the heterogeneous slopes during the simulated earthquake loading.

In the analysis, the nominal fragment size was defined as $d = \sqrt[2]{A_f/A_0}$, with A_f being the area of the fragment, and A_0 being the area of whole rock slope prior to seismic impact in a 2D analysis. Fig. 7 illustrates the distribution of fragment size with height within the slope. As shown in Fig. 7(a), the upper limit of fragment size decreased gradually with the increase of elevation within the slope (see the bold dashed line). A large number of fine fragments concentrated at the upper sector of the slope ridge, indicating lower confinement and intense slope fragmentation there. At the toe and upper sectors of the slope ridge, the fragment

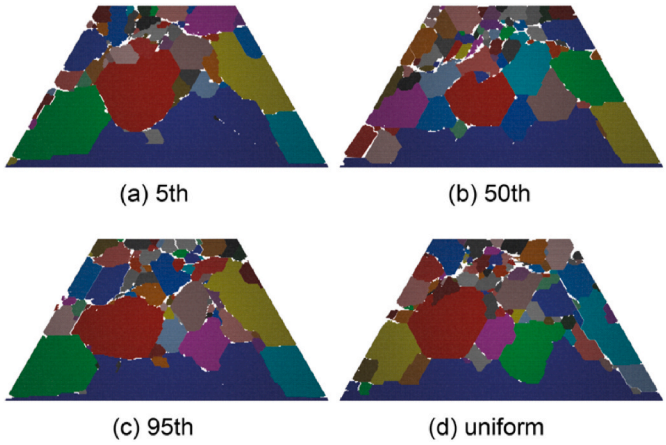

Fig. 6. Distribution of rock fragments at the end of the simulation for slopes of damage index at (a) 5th percentile; (b) 50th percentile; (c) 95th percentile in Fig. 5(b); (d) the uniform slope. The first few large fragments are coloured blue, red, green, yellow and cyan in order. The empty spaces within the slope profile are highly fragmented dispersed particles (not plotted). (For interpretation of the references to colour in this figure legend, the reader is referred to the Web version of this article.)

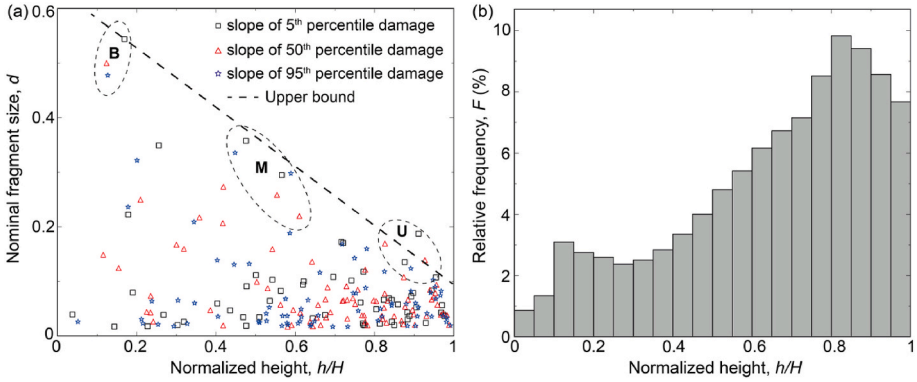

Fig. 7. (a) The distribution of nominal fragment size (d) along the height within the slope (h). The heigh is normalized by the initial slope height (H = 300 m). The number of data points for simulations at 5th, 50th, 95th percentiles of slope damage are 59, 78, 76, respectively; (b) the statistics of fragment number along the slope elevation for all simulations (in total 420,371 fragments were analysed). The regions **B**, **M** and **U** enclosed by the dashed curves show the points located at the bottom, middle and upper slope sectors.

size decreased gradually as the slope damage index increased from 5th to 95th percentiles (see the regions B and U in Fig. 7). However, in the middle region (M), such pattern is not clear. In general, the number of fragments increased quickly with the slope damage index due to the widespread internal fractures. As the damage index increases from 50th to 95th percentiles, there is a slight decrease in fragments number. This is mainly because at high slope damage, more fine particles and fragments (with less than 10 constituent particles) were produced, reducing the number of relatively large fragments. The statistics of fragments number along the height in Fig. 7(b) shows that the majority of rock fragments were concentrated at the upper sector of the slope. The fragments number reduced quickly towards the middle and base regions of the slope, indicating that the slope bedrock can largely maintain the initial intact structure during the earthquake loading.

Based on the identification of rock fragments after the earthquake event, the nominal fragment size distributions (FSD) for all tests can be analysed, as shown in Fig. 8(a). For different tests, the percentages of small fragments were very close, while large discrepancy existed for large fragments as controlled by the random fields of particle bonding strength. A significant mass percentage of relatively large (d > 0.1) fragments existed in these simulations, while they only amount to less than 30% in number. The numerical results can be best fitted by the Weibull's cumulative distribution function (WeibullCDF), as:

$$P = A\left(1 - e^{-(d/a)^b}\right) + P_0 \tag{8}$$

where P is the percentage of fragment size finer than the nominal size d; a, b, A and P_0 are fitting parameters.

As a comparison, Fig. 8(b) summarized the particle/fragment size distributions from site investigations on the freshly deposited Tangjiashan landslide dam in Southwest China,[50] on natural slopes in California[51] and recent landslide deposits in Taiwan.[52] All these studies were conducted in seismic active regions and thus can be considered comparable and useful to this research. It is evident that the natural debris fragments have widespread particle size distributions, which can also be best fitted by the Weibull's cumulative distribution function. As the current DEM simulations only focused on the relatively large debris fragments, Fig. 8(a) illustrates a very narrow range of FSD, similar to the data reported in Ref. 51 and Ref. 52. On the other hand, Chang & Zhang[50] focused on characterizing the geotechnical properties of soil deposits for a much wider range of particle sizes, and especially for a rock avalanche deposit where an additional fragmentation component is present due to long runout. Both numerical simulations of this study and site investigations indicate that the fragment size distribution of fractured slopes follows well the Weibull's cumulative distribution pattern.

For a practical analysis, the fragments of nominal size less than 0.1 or the cumulative mass percentage less than 20% can be considered as critical for hazard assessment, because small fragments located at the slope crest and surface (see Figs. 6 and 7) are more prone to collapse from the slope and generate landslides/rockfalls with respect to the larger ones. The small and shallow landslides have also been reported to have the highest occurrence frequency among all kinds of earthquake induced failures.[4,5] As shown in Fig. 9(a), in all tests, the cumulative mass percentage (P) of fragments with nominal size finer than 0.1 followed well the normal distribution pattern, with the majority distributed in the range of 12.1% (P_5) to 20.6% (P_{95}) of the total slope mass. The mean value of fragment mass percentage was 16.2%. For fine fragments of cumulative mass percentage less than 20%, the distribution of nominal size is shown in Fig. 9(b), which follow approximately the normal distribution with the mean value being 0.114. The fragments of an accumulative mass 20% of the slope had the nominal size less than 0.134 (d_{95}). Therefore, in designing the slopes or analysing related hazards, the 95th percentile values in these statistics (i.e. P_{95} and d_{95}) could be used to evaluate the rockfall/slide risks.

3.3. Energy evolution

Analysis of energy evolution is important for a comprehensive

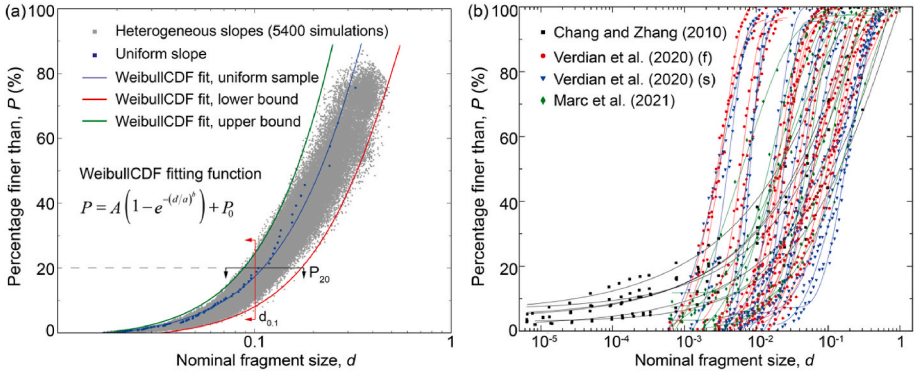

Fig. 8. (a) Fragment size distributions of RFT-DEM simulations. The fitting parameters for the Weibull CDF fittings are: for lower bound: a = 0.62, b = 1.5, A = 1.6, P_0 = −0.02; for upper bound: a = 0.48, b = 1.5, A = 2.9, P_0 = −0.02; uniform sample: a = 0.57, b = 1.4, A = 2.3, P_0 = −0.02. (b) The particle size distribution of Tangjiashan landslide site reported in Ref. 50 (6 curves); fracture spacing (f) and sediment size distributions reported in Ref. 51 (28 curves); grain size distributions reported in Ref. 52 (10 curves). The particle size/fracture spacing of each cited work were normalized by the largest size encountered in the series of tests of the three publications, 198.6 mm, 3291.9 mm and 3044.6 mm, respectively. The test data were best fitted by the Weibull CDF function.

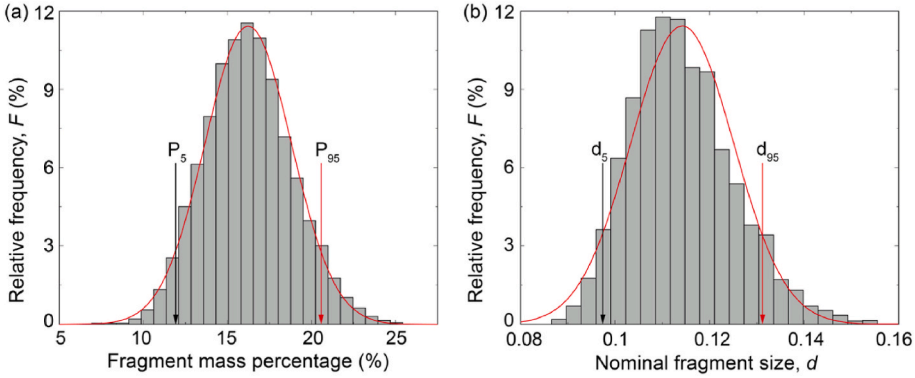

Fig. 9. (a) The statistics of fragment mass percentage with nominal fragment size finer than 0.1. $P_5 = 12.1\%$, $P_{95} = 20.6\%$. (b) The statistics of nominal fragment size with cumulative fragment mass up to 20% of the slope mass. $d_5 = 0.098$, $d_{95} = 0.134$.

understanding of the mechanisms of slope failure and post-failure landslide dynamics. Fig. 10 illustrates the evolutions of slope kinetic energy and fragmentation energy (energy released during the fracturing process) for simulations using different random fields. The kinetic energy increased and fluctuated slightly at the beginning of the simulation due to negligible ground accelerations (see Fig. 2). At the beginning, the heterogeneous and uniform slopes all exhibited the same pattern of kinetic energy evolution as no slope damage had occurred yet. After t = 0.5 s, the intense ground shaking led to the increase of slope kinetic energy, which quickly reached the peak value within a short time (~1 s). Correspondingly, induced slope damage also quickly approached the peak values (see Fig. 5). In this process, clear discrepancy of kinetic energy evolution occurred as determined by the geometry and dynamics of individual slope fragments. In general, once a rock fragment detached from the slope, its dynamics would be governed primarily by the gravity and collision with other fragments, instead of the earthquake loading. This was effectively a random process. Therefore, the evolutions of E_k for a series of simulations did not follow any clear pattern (see E_k of the uniform and heterogeneous slopes of 5th, 95th percentiles of damage index). After reaching the peak value, E_k decreased gradually with fluctuations. In this process, even though the energy input from seismic shaking at the slope base was still persistent, the energy dissipation due to bond breakage, friction and viscous damping between particles would lead to a significant reduction of the total kinetic energy (see Figure A1 in the Supplementary Information).

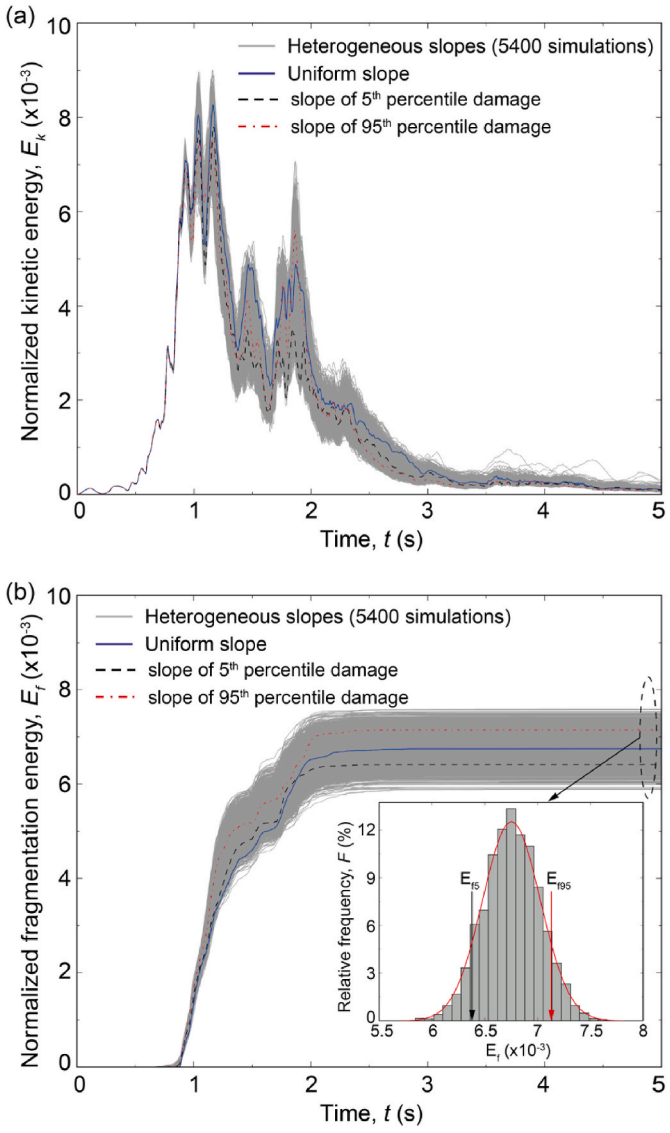

Fig. 10. Evolutions of (a) slope kinetic energy and (b) fragmentation energy over time for heterogeneous and uniform slopes. E_k: kinetic energy; E_f: slope fragmentation energy. The energy components are normalized by the total initial potential energy of the slope, E_{p0}.

Fig. 10(b) illustrates that the fragmentation energy (E_f) evolved similarly to the pattern of slope damage index in Fig. 5(a). The cumulative energy release due to bond breakage occurred mainly between 1 s and 2 s when the ground shaking was significant. The final fragmentation energy of each test can be more than 90% of the peak slope kinetic energy. For the series of tests, the frequency of final slope fragmentation energy followed well the normal distribution pattern. The statistical values of 5th and 95th percentiles of E_f (6.3×10^{-3} and 7.19×10^{-3}, respectively) were very close to the values in simulations of 5th and 95th percentiles of final slope damage index (i.e. = 6.4×10^{-3} and 7.15×10^{-3}, respectively). The slight difference was influenced by the properties of the broken bonds (e.g. location and strength).

3.4. Slope geometric effects

As discussed in Ref. 27, the mechanism of seismic amplification on slope surface could be the seismic velocity contrasts, which results in the trapping of seismic energy within the slope. This effect is largely controlled by the slope geometry and behaviour of seismic propagation, reflection and diffraction.[53] During earthquake, the enhanced slope deformation due to amplification has a significant impact on the slope fracturing process and associated rock strength degradation. Therefore, in this research the ground displacement amplification and slope fracturing patterns have been investigated in relation to the slope inclination angle, for the two testing conditions of fixed crest width and fixed

slope volume.

Similarly to the simulations presented in Section 3.1, the ground amplification effect was analysed via simulations using an idealized intact slope bonded with extremely high strengths. The amplification factor was defined as the ratio of peak ground acceleration at the crest (locations L, M and R in the inset plot of Fig. 11) to that at the centre of slope base (location B in the inset plot of Fig. 11). In this study, the seismic amplification factors at the left (A_L) and right (A_R) corners, and middle (A_M) of the slope crest were analysed to investigate the slope geometric effects. Fig. 11(a) illustrates that for simulations with fixed crest width, as the slope inclination angle increased, the amplification factors in the EW direction first increased and peaked at 40°. Then, the values decreased slightly and varied between 1.0 and 1.5. In the UD direction, A_L and A_R increased, while A_M decreased gradually with the slope angle. For simulations with fixed slope volume (Fig. 11(b)), similar trends had been observed, except that the peaks in the EW direction occurred at the gentlest angle of 30°.

The results indicate that gentle slopes could have higher amplifications than steep slopes in the EW direction, while in the UD direction it is lower. The ground accelerations at ridge corners can be amplified significantly (e.g. A_R and $A_M > 2.0$) when compared to the middle section of the crest ($A_M \approx 1.25$). The numerical results can match well the theoretical and numerical analyses in Ref. 53 that the peak amplification occurs preferably at the crest corner and gentle slopes generally have higher amplification factors than the steeper ones. The ground acceleration amplification and de-amplification alternated at crest surface due to the complex superposition of incident SV waves, reflected SV and P waves and diffracted Rayleigh waves. This is effectively controlled by the slope inclination angle, crest width and wavelength. A critical slope inclination angle of 32.3° with the strongest amplification has also been obtained in Ref. 53.

The influence of slope geometric effect on the fracturing process was investigated via simulations using breakable rock samples (i.e. the material properties were set the same as the uniform slope sample). The slope damage index and fragment size distributions are shown in Fig. 12. As shown in Fig. 12(a), for both type of tests, the slope damage index (D) decreased with the inclination angle, following the exponential relationships. *D* initially decreased slowly for slopes flatter than 60°, while it decreased quickly for steeper slopes. The tests with fixed slope volume had slightly higher damage index than those with fixed crest width. The results indicate that the steep slopes can better resist the earthquake induced fracturing with low damages. This is due to the local topographic effect that the steep slopes have much lower ground amplifications than the gentle slopes at the ridge crests (see Fig. 11). In addition, the widespread discontinuities in gentle slopes could also in turn increase the magnitude of ground displacement amplification.[27]

The fragment size distributions for different simulations are illustrated in Fig. 12(b) and Figure A3, A4 (see the Supplementary Information). Though slight discrepancy existed for gentle slopes, the fragment size distributions can be best fitted by the Weibull CDF function. As the inclination angle became higher, fewer fine fragments were produced. For slopes with inclination lower than 60°, the simulations using the fixed crest width condition produced more medium sized fragments (d = 0.05–0.2) than those using the fixed volume condition. This is due mainly to the relatively large slope volume used in the simulations with fixed crest width (see Figure A3 in Supplementary Information). Figure A3 also shows that as the inclination angle increased, the potential slope failure type transformed gradually from the toppling of local rock fragments close to the crest to the deep-seated giant landslide.

In the analysis, the cumulative energy dissipation (E_{diss}) and cumulative energy input into the slope mass by seismic loading ($E_{seismic}$) are defined as

$$E_{diss} = E_f + E_{fric} + E_d \tag{9}$$

$$E_{seismic} = E_p + E_k + \sum E_b + \sum E_c + E_{diss} - E_0 \tag{10}$$

where E_0 is the total energy of the initial slope prior to the seismic shaking, including the slope potential energy and elastic energy stored at the inter-particle bonds and contacts. The summation is over all particle bonds and contacts.

Fig. 13 illustrates the evolution of cumulative seismic input ($E_{seismic}$) and dissipated energy (E_{diss}) of the slopes under the testing conditions of (a) fixed crest width and (b) fixed slope volume. In all tests, $E_{seismic}$ was negligibly small before t = 0.5 s due to very small ground shaking. The energy dissipation only occurred after the initiation of bond breakage (t = 0.7–0.9 s), when fragmentation energy, frictional and damping dissipation energy began to increase. It is clear that the relative high value of $E_{seismic}$ at the beginning of the shaking initiated the slope damage. Then, the majority of seismic input energy transformed into the dissipated energy, as shown by the gradually converging trends for each respective test. Though slight discrepancy existed for the evolutions of these two types of energy in the middle of the simulation (t = 1–3 s), they were almost equal at the end of the ground shaking for any specific test. For simulations using fixed slope volume, the values of $E_{seismic}$ and E_{diss} increased quickly with the increase of slope inclination angle from 40° to 90°, while such a relationship was not clear for simulations using fixed crest width. The increases of $E_{seismic}$ and E_{diss} were due mainly to the high seismic energy input (see Figure A5 in the Supplementary Information) and slope damage (see Fig. 12(a)).

The numerical results indicate that the cumulative seismic input energy into the slope would finally be dissipated through the fracturing process and fragment interactions at discontinuities. Without any energy dissipation mechanism (e.g. strong rock mass with little or no bond

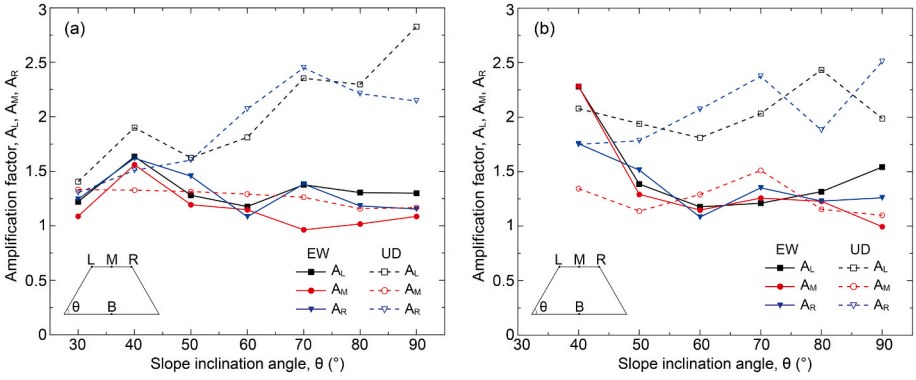

Fig. 11. Amplification of ground acceleration at the left (L), middle (M) and right (R) of the slope crest. The amplification factor is calculated as the ratio of peak ground accelerations at these locations to that at the slope base (location B). Both acceleration amplification in the EW and UD directions for tests with (a) fixed crest width and (b) slope volume were analyses.

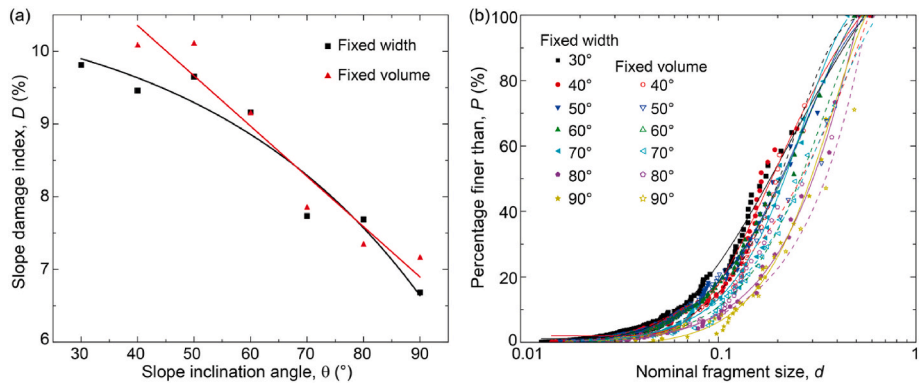

Fig. 12. (a) The influence of slope inclination angle on damage index. The results were best fitted by exponential function. (b) The fragment size distribution (FSD) for tests using different slope inclination angles. The FSD data were best fitted by the Weibull CDF function.

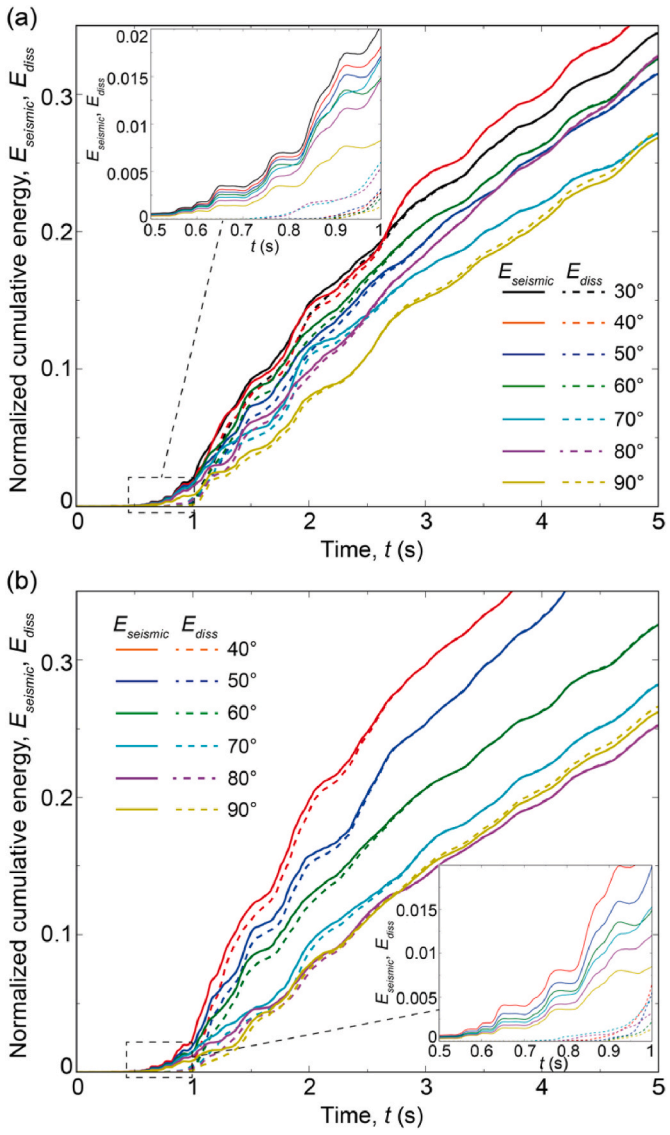

Fig. 13. Evolutions of cumulative seismic input energy ($E_{seismic}$) and cumulative energy dissipation (E_{diss}) for slopes of different inclination angles under the testing conditions of (a) fixed crest width and (b) fixed slope volume.

breakage), the slope should finally return to the original intact state after the earthquake and the cumulative seismic energy input would finally return to nil (see Figure A5). Thus, the overall bulk seismic energy input into the slope depends on the energy dissipation at discontinuities, such that the heavily fractured gentle slopes received more seismic energy than the steeper ones.

4. Discussion

This study aimed to illustrate the progressive fracturing process of heterogeneous rock slopes under transient earthquake loading by the coupled random field theory and discrete element modelling approach. Due to the high computational cost of modelling the slope topography in 3D DEM code, only the 2D DEM model was employed in this research. In addition, relatively large particles (~1.9–2.0 m) were employed in this study so that the field scale slope was generated using a relatively small number of particles in DEM. This approach has significantly reduced the overall computational cost. The use of parallel bond model between large particles in DEM can effectively mimic the intact rock bridges and slope mass. The very narrow particle grading instead of a wide size range can reduce the material uncertainty and inhomogeneity introduced by the irregular particle packing matrix. The small polydispersity of particle grading was adopted to avoid the particle crystallization in DEM simulations. The presented results revealed that the fracturing process of a heterogeneous slope can be reproduced, at least in a reasonably qualitative way by the breakage of interparticle bonds. However, when applying such an idealized model configuration (e.g. simple geometry and loading conditions) to field studies, problems may arise as to what extent the simple 2D DEM modelling and a short-term single transient strong earthquake event are representative of real slope topography and loading conditions.

4.1. Modelling timescale and boundary condition

In this study, the modelling timescale was set to 5-s, while in reality the earthquake shaking period was 50 s, as a compromise of computational cost in the massive DEM simulations. The simulations were run on a Desktop Workstation (i.e. Intel Xeon Processor W-2255 (10C, 3.7 GHz 4.7 GHz Turbo HT 19.25 MB 165 W DDR4-2933)). A single simulation took 2 CPU hours and the whole 5400 simulations in this research required 10800 CPU hours to complete. By using the parallel simulation technique, 10 simulations were run in parallel at the same time, and the whole simulation series took around 45 days. In the DEM simulations, since the iteration time step (5×10^{-4} s) was set 10 times smaller than the real seismic signal incremental (5×10^{-3} s), the DEM simulations were effectively speeded up by 10 times. This approach could numerically achieve the same ground displacement as the real strong earthquake within a short period of time (e.g. 5 s). In fact, the scaling of

modelling time has been widely adopted in DEM to make the computational cost acceptable using the existing computing resources.[54,55]

In addition, during the seismic shaking, the ground acceleration can be amplified significantly at the slope surface due to wave reflection and diffraction by slope topography irregularities.[56] As a result, the slope crest and surface tend to be fractured thoroughly. Accurate evaluation of ground amplification effect is complicated if slope topography, soil properties, frequency and angle of incident seismic wave are considered simultaneously in the simulations. To simplify the analysis, this research only employed an idealized slope geometry and uniform particle size grading. The DEM model can effectively capture the progressive slope fracturing process under continuous ground shaking at a relatively low computational cost. It is assumed that this approach can provide useful information of seismic induced slope fracturing. During DEM simulations, a relatively high viscous damping coefficient (0.5) was employed at the slope base to reduce the ground amplification due to the reflection of long wavelength seismic waves at the rigid basal boundary. This numerical technique effectively mimics an absorbing boundary condition, in which energy of reflected waves at the base can be absorbed.[28]

4.2. Slope fragmentation characteristics

The DEM simulations in this study revealed that the rock mass can be heavily fragmented under the intense seismic loading. In this process, the internal cracks propagated and nucleated within the slope, interrupting the transmission of stress waves and leading to significant energy dissipation at the discontinuities. The resulting fragment size decreased with the height within the slope and the fine fragments concentrated mainly at the slope crest, as illustrated in Figs. 6 and 7 and Figure A3 (in the Supplementary Information). In general, near the slope surface, intense superposition of incident SV waves, reflected SV and P waves, and Rayleigh waves exists, which increases the amplitude of resultant waves as the energy piles up. As reported in Ref. 57, the generated Rayleigh wave at the crest can have the amplitudes 0.4 times as much as the incident waves. The slope topography can further increase the amplification effect.[56] Depending on the location and material properties (e.g. rock strength) at different locations of a heterogeneous slope, the ground amplification intensity varies widely, facilitating the occurrence of differential ground displacement. In addition, the fracturing probability of a rock mass is primarily controlled by its tensile strength.[28] Thus, the relatively low strengths and high ground amplifications at the slope crest and surface could the dominant factors controlling the fragment sizes.

The slope topography can have a significant influence on the fragmentation process, due primarily to ground amplification effects. The gentler slopes generally have higher amplification than the steeper ones, such that the slope were more intensely fragmented with a large number of fine fragments at the crest and slope surface along the height of the slope (see Figure A3 in the Supplementary Information). When compared to the steeper ones, the gentler slopes have much longer inclined slope lengths at low reliefs and the UD seismic wave only needs to travel shorter distances to reach the slope surfaces with less energy loss. The reflected P waves can directly reach the upper surface and superimpose with the SV and Rayleigh waves. Correspondingly, a large portion of seismic energy can reach the slope surface and be amplified due to wave superposition. This process can lead to both higher amplitudes and longer duration of shaking. Therefore, seismic wave of high energy together with the differential ground displacement can heavily damage the upper sector of the slope. For steeper slopes, this effect is significantly weakened as the reflected P waves transform into surface waves and their amplitudes quickly reduce to zero.[53] As a result, the steep slopes have much lower fragmentation intensity and only several major interconnected cracks existed within the slope. These fracturing patterns could control subsequent slope failure/landslide dynamics, such that small scale landslide can occur in gentle slopes, while deep-seated giant landslides can happen in steep slopes.

4.3. Multiple earthquake impacts

The current study only focused on the impact of a single transient strong earthquake on slope fracturing, while in nature, earthquakes of various magnitudes may happen periodically in a specific region. These repeated earthquakes with strong cyclic loading and unloading effects can induce significant incremental internal damage of rock slope overtime. As stated in Ref. 23, the seismic-induced slope fracturing process can selectively open existing joints and reduce the normal stiffness of rock fragments, which results in strong spectral amplification when subsequent earthquakes occur. This process can also lead to intense stress variations within the rock mass and between the pre-existing fracture networks. These compliant fractures would finally bring the rock slope to a highly critical state, at which an even small disturbance, e.g. low-magnitude earthquake or rainfall, combined with the localized ground amplification and site effects, may lead to the ultimate catastrophic failure of the slope.[15,58,59] This effect is particularly significant for deep-seated landslides as characterized by the long-term and time-dependent creeping movement, but short periods of rapid accelerations at failure. The failure surface normally consists of pre-existing shear planes and newly formed fractures. A good example can be the large number of slope failures occurred in the Wenchuan seismic zone resulting from the long-term active tectonic activities and repeated earthquakes. These historical seismic events could be the destabilization mechanisms contributing to the impending slope failures or the preparatory ones for a triggering rainfall event.

As the primary objective of this study was to investigate the mechanism of slope fracturing with heterogeneous initial material properties, only a single transient earthquake event was analysed. However, the DEM modelling presented has already shown the capability to qualitatively capture the characteristic of progressive slope fracturing, including evolution of fracture network, damage index and slope fragmentation energy, the distributions of fragment sizes and ground amplification effect. The current study can be further extended to the study of multiple earthquake impacts, with explicit consideration of material heterogeneity and with different magnitudes.

5. Conclusions

The earthquake induced slope fracturing process was investigated by a novel probabilistic modelling approach combining the random field theory and discrete element method. This approach enables the heterogeneity of slope material strength to be explicitly quantified by the random field theory in a standard normal distribution. The simplified 2D model configuration can effectively analyse the feedbacks between progressive slope fracturing and seismic site effects. The slope fracturing occurred naturally when the imposed seismic loads exceeded the bonding strength of particles in DEM modelling. The statistical results of rock fragment size, damage index and slope energy components can provide useful information for slope designs and rockfall hazard evaluations. The major findings are summarized as follows:

1) The ground amplification was significant at the slope crest and ground surface, with the cumulative displacement up to 8 times the base shaking displacement. Differential ground displacements at the same slope height existed widely within the slope, which is the triggering factor of slope fracturing.
2) As the ground acceleration increased, the small fractures first occurred at the slope surface near the crest region, quickly propagating and nucleating within the slope to form interconnected larger fractures. The major slope damages occurred within a short period of time (1 s) when the large ground displacements dominated (≈0.2 m). Depending on the initial random fields of rock strength, these fractures concentrated primarily at the upper sector of the slope, while the bottom region of the slope remained intact.

3) The size of the generated rock fragments followed well the Weibull's cumulative distribution. It decreased with the height within the slope. The slope fragmentation energy has been introduced to quantify the energy release during the fracturing process. For the series of tests, the slope fragmentation energy followed the normal distribution.
4) The slope inclination angle could influence the fracturing process significantly. Both the ground amplification and slope damage index decreased with the increase of inclination. The cumulative seismic energy input into the slope increased with the increase of slope inclination and would finally be dissipated through the fracturing process and fragment interactions at discontinuities.

Declarations

The authors declare that they have no conflict of interest. This is an original paper which has neither previously been published, nor under consideration for publication anywhere else; that its publication has been approved by all co-authors. All the data is authentic and was developed by the authors.

Declaration of competing interest

The authors declare that they have no known competing financial interests or personal relationships that could have appeared to influence the work reported in this paper.

Acknowledgements

This research was supported, in whole or in part, by the *UK Engineering and Physical Sciences Research Council (EPSRC) New Investigator* Award (grant EP/V028723/1), the *Royal Society*, *Sino-British Fellowship Trust International Exchanges* Award (grant IES\R2\202023) and the open funding of the State Key Laboratory of Water Resources and Hydropower Engineering Science (Wuhan University) (grant 2019SGG02). The Fondazione Cariplo project @RockHoRiZon – Advanced Tools for Rockfall Hazard and Risk zonation at the regional scale supported GC.

A CC BY or equivalent licence is applied to that at least the Author Accepted Manuscript (AAM) arising from this submission, in accordance with the grant's open access conditions.

The data of this study are publicly available online (https://figshare.com/s/bdc2051f08d477988bba).

Appendix A. Supplementary data

Supplementary data to this article can be found online at https://doi.org/10.1016/j.ijrmms.2022.105171.

References

1 Fan X, Scaringi G, Korup O, et al. Earthquake-induced chains of geologic hazards: patterns, mechanisms, and impacts. *Rev Geophys*. 2019;57(2):421–503. https://doi.org/10.1029/2018RG000626.
2 Huang RQ, Li WL. Analysis of the geo-hazards triggered by the 12 may 2008 Wenchuan earthquake, China. *Bull Eng Geol Environ*. 2009;68(3):363–371. https://doi.org/10.1007/s10064-009-0207-0.
3 Keefer DK. The importance of earthquake-induced landslides to long-term slope erosion and slope-failure hazards in seismically active regions. *Geomorphology*. 1994;10(1):265–284.
4 Yagi H, Sato G, Higaki D, Yamamoto M, Yamasaki T. Distribution and characteristics of landslides induced by the Iwate–Miyagi Nairiku earthquake in 2008 in Tohoku district, Northeast Japan. *Landslides*. 2009;6(4):335. https://doi.org/10.1007/s10346-009-0182-3.
5 Khazai B, Sitar N. Evaluation of factors controlling earthquake-induced landslides caused by Chi-Chi earthquake and comparison with the Northridge and Loma Prieta events. *Eng Geol*. 2004;71(1):79–95. https://doi.org/10.1016/S0013-7952(03)00127-3.
6 Gischig V, Preisig G, Eberhardt E. Numerical investigation of seismically induced rock mass fatigue as a mechanism contributing to the progressive failure of deep-seated landslides. *Rock Mech Rock Eng*. 2016;49(6):2457–2478. https://doi.org/10.1007/s00603-015-0821-z.
7 Crosta GB, Imposimato S, Roddeman D, Chiesa S, Moia F. Small fast-moving flow-like landslides in volcanic deposits: the 2001 Las Colinas Landslide (El Salvador). *Eng Geol*. 2005;79(3):185–214. https://doi.org/10.1016/j.enggeo.2005.01.014.
8 Keefer DK. Landslides caused by earthquakes. *GSA Bulletin*. 1984;95(4):406–421.
9 Kokusho T, Ishizawa T. Energy approach to earthquake-induced slope failures and its Implications. *J Geotech Geoenviron Eng*. 2007;133(7):828–840. https://doi.org/10.1061/(ASCE)1090-0241(2007)133, 7(828).
10 Post. Effects of the March 1964 Alaska earthquake on glaciers: U.S. Geological survey professional paper 544–D. Retrieved from https://pubs.usgs.gov/pp/0544d/; 1967.
11 Valagussa A, Marc O, Frattini P, Crosta GB. Seismic and geological controls on earthquake-induced landslide size. *Earth Planet Sci Lett*. 2019;506:268–281.
12 Meunier P, Hovius N, Haines AJ. Regional patterns of earthquake-triggered landslides and their relation to ground motion. *Geophys Res Lett*. 2007;34(20).
13 Meunier P, Hovius N, Haines JA. Topographic site effects and the location of earthquake induced landslides. *Earth Planet Sci Lett*. 2008;275(3):221–232.
14 Valagussa A, Frattini P, Crosta GB. Earthquake-induced rockfall hazard zoning. *Eng Geol*. 2014;182:213–225. https://doi.org/10.1016/j.enggeo.2014.07.009.
15 Marc O, Hovius N, Meunier P, Uchida T, Hayashi S. Transient changes of landslide rates after earthquakes. *Geology*. 2015;43(10):883–886. https://doi.org/10.1130/G36961.1.
16 Huang R, Fan X. The landslide story. *Nat Geosci*. 2013;6(5):325–326.
17 Valagussa A, Frattini P, Valbuzzi E, Crosta GB. Role of landslides on the volume balance of the Nepal 2015 earthquake sequence. *Sci Rep*. 2021;11(1):3434.
18 Lin G, Chen H, Chen Y, Horng M. Influence of typhoons and earthquakes on rainfall-induced landslides and suspended sediments discharge. *Eng Geol*. 2008;97(1):32–41.
19 Muñoz-Torrero Manchado A, Allen S, Ballesteros-Cánovas JA, Dhakal A, Dhital MR, Stoffel M. Three decades of landslide activity in western Nepal: new insights into trends and climate drivers. *Landslides*. 2021;18(6):2001–2015. https://doi.org/10.1007/s10346-021-01632-6.
20 Owen LA, Kamp U, Khattak GA, Harp EL, Keefer DK, Bauer MA. Landslides triggered by the 8 october 2005 Kashmir earthquake. *Geomorphology*. 2008;94(1):1–9.
21 Tian Y, Owen LA, Xu C, et al. Landslide development within 3 years after the 2015 Mw 7.8 Gorkha earthquake, Nepal. *Landslides*. 2020;17(5):1251–1267. https://doi.org/10.1007/s10346-020-01366-x.
22 Croissant T, Steer P, Lague D, Davy P, Jeandet L, Hilton RG. Seismic cycles, earthquakes, landslides and sediment fluxes: linking tectonics to surface processes using a reduced-complexity model. *Geomorphology*. 2019;339:87–103.
23 Moore, Burjánek J, et al. In: Eberhardt E, Froese C, Turner K, Leroueil S, eds. *Earthquake-triggered Rock Slope Failures. Damage and Site Effects*. CRC Press; 2012:875. Retrieved from http://hdl.handle.net/20.500.11850/61211.
24 Palmer J. Creeping earth could hold secret to deadly landslides. *Nature*. 2017;548(7668):384–386.
25 Utili S, Crosta GB. Modeling the evolution of natural cliffs subject to weathering: 1. Limit analysis approach. *J Geophys Res: Earth Surf*. 2011;116.
26 Tran TV, Alkema D, Hack R. Weathering and deterioration of geotechnical properties in time of groundmasses in a tropical climate. *Eng Geol*. 2019;260, 105221.
27 Gischig VS, Eberhardt E, Moore JR, Hungr O. On the seismic response of deep-seated rock slope instabilities — insights from numerical modeling. *Eng Geol*. 2015;193:1–18. https://doi.org/10.1016/j.enggeo.2015.04.003.
28 Zhao T, Crosta GB. On the dynamic fragmentation and lubrication of coseismic landslides. *J Geophys Res Solid Earth*. 2018;123(11):9914–9932.
29 Griffiths DV, Jinsong H, Fenton Gordon A. Influence of spatial variability on slope reliability using 2-D random fields. *J Geotech Geoenviron Eng*. 2009;135(10):1367–1378. https://doi.org/10.1061/(ASCE)GT.1943-5606.0000099.
30 Liu Y, Lee F, Quek S, Beer M. Modified linear estimation method for generating multi-dimensional multi-variate Gaussian field in modelling material properties. *Probabilist Eng Mech*. 2014;38:42–53. https://doi.org/10.1016/j.probengmech.2014.09.001.
31 Zhao T, Liu Y. A novel random discrete element analysis of rock fragmentation. *Int J Numer Anal Methods GeoMech*. 2020;44(10):1386–1395. https://doi.org/10.1002/nag.3067.
32 Weatherley D, Boros V, Hancock W. *ESyS-Particle Tutorial and User's Guide Version 2.1*. Brisbane: Earth Systems Science Computational Centre, The University of Queensland; 2011.
33 Potyondy DO, Cundall PA. A bonded-particle model for rock. *Int J Rock Mech Min Sci*. 2004;41(8):1329–1364.
34 Wang Y. A new algorithm to model the dynamics of 3-D bonded rigid bodies with rotations. *Acta Geotechnica*. 2009;4(2):117–127. https://doi.org/10.1007/s11440-008-0072-1.
35 Zhao T, Crosta GB, Utili S, De Blasio FV. Investigation of rock fragmentation during rockfalls and rock avalanches via 3-D discrete element analyses. *J Geophys Res: Earth Surf*. 2017;122(3):678–695. https://doi.org/10.1002/2016JF004060.
36 Utili S, Zhao T, Houlsby GT. 3D DEM investigation of granular column collapse: evaluation of debris motion and its destructive power. *Eng Geol*. 2015;186:3–16.
37 Hoek E, Bray JD. *Rock Slope Engineering*. London: CRC Press; 1981.
38 Elsen PR, Tingley MW. Global mountain topography and the fate of montane species under climate change. *Nat Clim Change*. 2015;5(8):772–776. https://doi.org/10.1038/nclimate2656.
39 Shen H, Abbas SM. Rock slope reliability analysis based on distinct element method and random set theory. *Int J Rock Mech Min Sci*. 2013;61:15–22.
40 Yin Y, Wang F, Sun P. Landslide hazards triggered by the 2008 Wenchuan earthquake, Sichuan, China. *Landslides*. 2009;6(2):139–152. https://doi.org/10.1007/s10346-009-0148-5.
41 Miščević P, Vlastelica G. Impact of weathering on slope stability in soft rock mass. *J Rock Mech Geotech Eng*. 2014;6(3):240–250.

42 Villeneuve MC, Heap MJ, Kushnir ARL, et al. Estimating in situ rock mass strength and elastic modulus of granite from the Soultz-sous-Forêts geothermal reservoir (France). *Geoth Energy*. 2018;6(1):11. https://doi.org/10.1186/s40517-018-0096-1.

43 Meng Q, Zhang M, Han L, Pu H, Nie T. Effects of Acoustic emission and energy evolution of rock specimens under the uniaxial cyclic loading and unloading compression. *Rock Mech Rock Eng*. 2016;49(10):3873–3886. https://doi.org/10.1007/s00603-016-1077-y.

44 Bell. Engineering geology | problematic rocks. In: Selley RC, Cocks LRM, Plimer IR, eds. *Encyclopedia of Geology*. Oxford: Elsevier; 2005:543–554. Retrieved from https://www.sciencedirect.com/science/article/pii/B0123693969002203.

45 Hu Y, Wang Y. Probabilistic soil classification and stratification in a vertical cross-section from limited cone penetration tests using random field and Monte Carlo simulation. *Comput Geotech*. 2020;124, 103634. https://doi.org/10.1016/j.compgeo.2020.103634.

46 Liu C, Chen C. Spatial correlation structures of CPT data in a liquefaction site. *Eng Geol*. 2010;111(1):43–50. https://doi.org/10.1016/j.enggeo.2009.12.002.

47 Brigid C, Sina J, Kok-Kwang Phoon, Jianye C. Scale of fluctuation for spatially varying soils: estimation methods and values. *ASCE-ASME Journal of Risk and Uncertainty in Engineering Systems, Part A: Civ Eng*. 2020;6(4), 03120002. https://doi.org/10.1061/AJRUA6.0001083.

48 Griffiths DV, Fenton GA, Denavit MD. *Traditional and Advanced Probabilistic Slope Stability Analysis*. 2007. https://doi.org/10.1061/40914(233)19.

49 Xu Q, Li Y, Zhang S, Dong X. Classification of large-scale landslides induced by the 2008 Wenchuan earthquake, China. *Environ Earth Sci*. 2015;75(1):22. https://doi.org/10.1007/s12665-015-4773-0.

50 Chang DS, Zhang LM. Simulation of the erosion process of landslide dams due to overtopping considering variations in soil erodibility along depth. *Nat Hazards Earth Syst Sci*. 2010;10(4):933–946. https://doi.org/10.5194/nhess-10-933-2010.

51 Verdian JP, Sklar LS, Riebe CS, Moore JR. Sediment size on talus slopes correlates with fracture spacing on bedrock cliffs: Implications for predicting initial sediment size distributions on hillslopes. *Earth Surface Dynamics, 2020*. 2020:1–23. https://doi.org/10.5194/esurf-2020-54.

52 Marc O, Turowski JM, Meunier P. Controls on the grain size distribution of landslides in Taiwan: the influence of drop height, scar depth and bedrock strength. *Earth Surf Dyn*. 2021;9(4):995–1011. https://doi.org/10.5194/esurf-9-995-2021.

53 Zhang Z, Fleurisson J, Pellet F. The effects of slope topography on acceleration amplification and interaction between slope topography and seismic input motion. *Soil Dynam Earthq Eng*. 2018;113:420–431. https://doi.org/10.1016/j.soildyn.2018.06.019.

54 Feng YT, Owen DRJ. Discrete element modelling of large scale particle systems—I: exact scaling laws. *Computational Particle Mechanics*. 2014;1(2):159–168.

55 Hassan S, El Shamy U. DEM simulations of the seismic response of granular slopes. *Comput Geotech*. 2019;112:230–244. https://doi.org/10.1016/j.compgeo.2019.04.019.

56 Jafarzadeh F, Shahrabi MM, Farahi Jahromi H. On the role of topographic amplification in seismic slope instabilities. *J Rock Mech Geotech Eng*. 2015;7(2):163–170. https://doi.org/10.1016/j.jrmge.2015.02.009.

57 Boore DM, Harmsen SC, Harding ST. Wave scattering from a step change in surface topography. *Bull Seismol Soc Am*. 1981;71(1):117–125.

58 Rosser N, Kincey M, Oven K, et al. Changing significance of landslide hazard and risk after the 2015 Mw 7.8 Gorkha, Nepal earthquake. *Progress in Disaster Science*. 2021;10, 100159.

59 Zhang S, Zhang L, Lacasse S, Nadim F. Evolution of mass movements near epicentre of Wenchuan earthquake, the first eight years. *Sci Rep*. 2016;6(1), 36154.